ACS APPLIED MATERIALS & INTERFACES

www.acsami.org

Research Article

Surface Passivation to Enhance the Interfacial Pyro-Phototronic Effect for Self-Powered Photodetection Based on Perovskite Single Crystals

Linjuan Guo, Yi Song, Baorong Wang, Ridong Cong, Lei Zhao, Suheng Zhang, Leipeng Li, Wenqiang Wu, Shufang Wang, Xingyuan San,* Caofeng Pan,* and Zheng Yang*

Cite This: *ACS Appl. Mater. Interfaces* 2024, 16, 16482−16493

Read Online

ACCESS | Metrics & More | Article Recommendations | Supporting Information

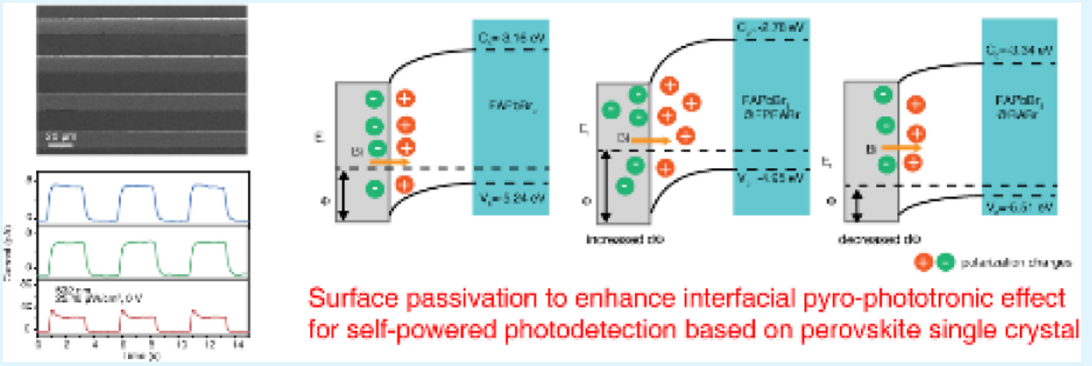

ABSTRACT: The interfacial pyro-phototronic effect (IPPE) presents a novel approach for improving the performance of self-powered photodetectors (PDs) based on metal halide perovskites (MHPs). The interfacial contact conditions within the Schottky junctions are crucial in facilitating the IPPE phenomenon. However, the fabrication of an ideal Schottky junction utilizing MHPs is a challenging endeavor. In this study, we present a surface passivation method aimed at enhancing the performance of self-powered photodetectors based on inverted planar perovskite structures in micro- and nanoscale metal-halide perovskite SCs. Our findings demonstrate that the incorporation of a lead halide salt with a benzene ring moiety for surface passivation leads to a substantial improvement in photoresponses by means of the IPPE. Conversely, the inclusion of an alkane chain in the salt impedes the IPPE. The underlying mechanism can be elucidated through an examination of the band structure, particularly the work function (WF) modulated by surface passivation. Consequently, this alteration affects the band bending and the built-in field (V_{Bi}) at the interface. This strategy presents a feasible and effective method for producing interfacial pyroelectricity in MHPs, thus facilitating its potential application in practical contexts such as energy conversion and infrared sensors.

KEYWORDS: *interfacial pyro-phototronic effect, surface passivation, self-powered photodetectors, metal halide perovskites, single crystals*

1. INTRODUCTION

Photodetectors (PDs) are optoelectronic devices that serve a crucial function in diverse domains, such as optical communication, optical guidance technology, and environmental monitoring, by converting light into electrical signals.[1−4] Self-powered PDs are highly sought after for sensing in extreme conditions such as environmental sensing, chemical sensing, and biosensing. This is due to their advantageous features of wireless operation, maintenance-free functionality, and absence of external power requirements. Furthermore, the integration of self-powered PDs with other electronic devices, such as biomedical diagnostics and intelligent sensing systems, allows them to serve as a power supply in addition to their sensing capabilities.[5−7] In order to produce high-performance PDs that exhibit high responsivity (R), high external quantum efficiency (EQE), low dark current, and fast response speed, it is imperative that the light-absorbing materials possess a high absorption coefficient, low trap-state density, high carrier mobility, and a low carrier recombination rate. Additionally, the fabrication of PDs on a large scale, at a low cost, and without the need for complex equipment is essential in light of the pressing concerns surrounding global environmental pollution and the imperative for carbon neutrality.

Received: January 6, 2024
Revised: March 6, 2024
Accepted: March 12, 2024
Published: March 20, 2024

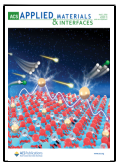

Metal halide perovskites (MHPs) have demonstrated significant potential in various fields such as solar cells, PDs, light-emitting diodes (LEDs), and lasers in recent years. This is primarily attributed to their exceptional photoelectric properties, straightforward and cost-effective processing methods, as well as their ability to adjust the bandgap according to specific requirements.[8−11] Due to these aforementioned advantages, MHPs are widely regarded as highly suitable candidates for future self-powered PDs. The single crystals (SCs) of MHPs exhibit significantly enhanced optical and electrical properties, as well as improved stability in comparison to their polycrystalline counterparts. Consequently, numerous high-performance PDs have been reported, which are based on MHP SCs.[12−14] The fabrication of self-powered PDs for MHP polycrystalline films can be achieved with relative ease by employing solar cell-like structures such as p−i−n junctions or pn junctions.[15,16] However, the fabrication of an optimal Schottky junction or heterojunction for self-powered photodetectors based on MHPs is a complex task due to the significant degradation of MHPs during a conventional lithographic procedure.[17] Hence, the operation of PDs typically necessitates the inclusion of a voltage bias. Various physical phenomena, such as the ferroelectric effect and piezo-phototronic effect, can independently or collectively influence the band structure modulation of a Schottky junction or heterojunction.[18−20]

The pyro-phototronic effect, which involves the interplay of pyroelectricity, photoexcitation, and semiconductors, has recently been utilized in the development of self-powered PDs based on ferroelectric MHPs.[21−27] However, the utilization of the pyro-phototronic effect in nonpolar perovskites is frequently constrained. Recent findings have indicated that centrosymmetric materials possess the capability to manifest pyroelectricity at the interface with alternative materials. Yang et al. conducted a study that showcased the generation of interfacial piezoelectric and pyroelectric effects through the built-in electric field within the depletion region of the Schottky contact interface.[28] Ahmadi et al. demonstrated a silicon-water heterostructure-based PD relying on the interfacial pyro-phototronic effect (IPPE).[29] The IPPE relies on the change of intensity of interfacial polarization, which is induced by band bending at the junction interface. In our previously conducted research, it was observed that the contact conditions, including the selection of metals and surface smoothness, significantly influence the IPPE.[30] Just by finely polishing the SCs or growing the SCs on the preprepared semiconductor or electrodes, it is possible to achieve desirable photoresponses induced by pyroelectric effects. However, when dealing with micro- or nanoscale MHP SCs, these procedures become intricate. Consequently, there is a pressing need to establish a universal and convenient approach for implementing the interface passivation technique in micro- or nanoscale MHP SCs. Recently, the implementation of surface passivation holds significant potential in mitigating interface charge recombination and enhancing the stability of MHPs.[31−34] Furthermore, numerous reports have provided evidence that the introduction of specific functional groups can induce passivation, resulting in band bending at the surface of the perovskite materials. This phenomenon effectively enhances the separation of charge carriers, suppresses recombination, and ultimately contributes to the improved efficiency of solar cells.[35−37] Consequently, it is anticipated that surface passivation confers advantages to IPPE, which are instigated by interface band bending.

In this study, a surface passivation technique was employed to improve the performance of IPPE-based self-powered PDs in micro- and nanoscale MHP SCs. The results indicate that the use of a lead halide salt containing a benzene ring group for surface passivation significantly enhances the photoresponses through the pyro-phototronic effect. Conversely, the presence of an alkane chain in the salt hampers the interfacial pyroelectric effect. Through the utilization of theoretical calculations, various techniques such as ultraviolet photoelectron spectroscopy (UPS), capacitive−voltage ($C-V$), and kelvin probe force microscope (FPFM), our investigation has revealed that the inclusion of benzene ring groups in MHP SCs can effectively decrease the WF. Consequently, this reduction induces a more pronounced bending of the band structure at the MHP/metal Schottky contact, thereby enhancing the interfacial polarization and ultimately improving the pyroelectric photoresponses. Furthermore, this approach is widely applicable across various 3D MHPs. This research presents a straightforward and efficient technique for augmenting the IPPE in perovskite SCs, rendering perovskite Schottky junctions a compelling choice for high-performance self-powered PDs.

2. EXPERIMENTAL SECTION

2.1. Materials. The *N*,*N*-dimethylformamide (DMF, 99.9%), *N*-cycloethylpyrrolidone (CHP, 99.9%), 4-fluorophenethylamine (99%), 3,4,5-trifluorobenzylamine (97%), hydrobromic acid (HBr, 48 wt %, 99.9%), cyclohexane (99.5), *tert*-amyl alcohol (99.5%), 3-(bromopropyl)trimethoxysilane (99%), and 3-(chloropropyl)-trimethoxysilane (99%) were purchased from Shanghai Macklin Biochemical Co., Ltd. Formamidinium bromide (FABr, 99.99%), methylamine bromide (MABr, 99.99%), *n*-butylamine bromide (BABr, 99.99%), phenylethylamine bromide (PEABr, 99.99%), lead bromide ($PbBr_2$, 99.99%), and lead chloride ($PbCl_2$, 99.99%) were purchased from Xi'an Yuri Solar Co., Ltd. 4-FPEABr and 345-FAnBr were obtained by the reaction between the corresponding amine with the HBr. Lead chloride ($PbCl_2$, 99.99%) and benzylamine hydrochloride (PMACl, 99.99%) were Sylgard 184 poly(dimethylsiloxane) (PDMS) prepolymer was purchased from DOWSIL. All the chemicals were used as received without further purification.

2.2. Preparation of PDMS Templates. Patterned rectangular SU-8 arrays on the Si/SiO_2 substrates with a thickness of 1 μm were performed by conventional UV lithography using a SU-8 photoresist (MicroChem 2000.5). PDMS solution was prepared by mixing a 10:1 ratio of PDMS prepolymer and the cross-linking agent, casting onto the as-prepared SU-8 arrays, and being cured at 80 °C for 3 h. Finally, the PDMS template with a thickness of 1 cm was peeled off and cut into 1 cm × 1 cm pieces for further use.

2.3. Growth of Three MHP SCs. The $FAPbBr_3$ and $MAPbBr_3$ MMBs were prepared by using a PDMS template-assisted cosolvent evaporation method. In brief, 5 μL of precursor solution (1 M FABr or MABr and 0.5 M $PbBr_2$ in DMF/CHP with a volume ratio of 9:1) was dropped on 3-(bromopropyl)trimethoxysilane-treated hydrophobic SiO_2/Si substrate (1 cm × 1 cm). Then, the PDMS template was brought into contact with the DMF solution. Uniform pressure was applied by using an adjustable clamp. Then the clamp was transferred into the glovebox for full evaporation of the solvent. For $MAPbCl_3$ MFs, a space-confined ITC method was used.

2.4. Cleaning and Passivation of the MHPs. Briefly, the cleaning solutions were prepared by mixing cyclohexane and *tert*-amyl alcohol in a volume ratio of 4:1. The passivation solutions were prepared by dissolving 0.2 mg mL^{-1} of FABr, BABr, OABr, 4-FPEABr, PEABr, or 345FAnBr in the cleaning solution. For bare $FAPbBr_3$ MMBs, only a cleaning procedure was conducted.

https://doi.org/10.1021/acsami.4c00302
ACS Appl. Mater. Interfaces 2024, 16, 16482−16493

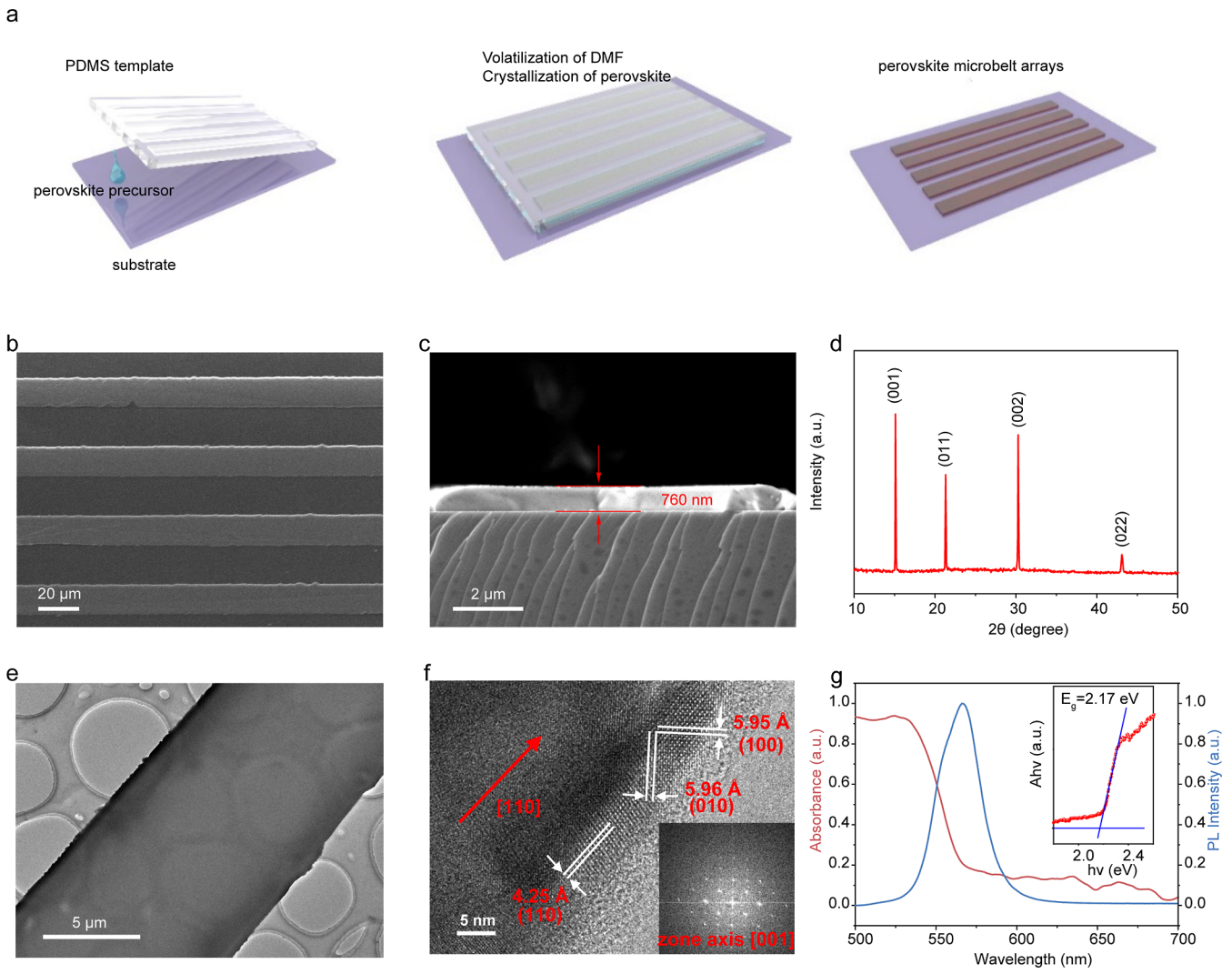

Figure 1. Characterizations of $FAPbBr_3$ MMB arrays. (a) Schematic illustration of the growth procedures using the PDMS-templated space-confined method. (b) Top-view SEM image, (c) cross-sectional SEM image, and (d) XRD pattern of the $FAPbBr_3$ MMB arrays. (e) Low-magnified TEM image, (f) HRTEM image, and corresponding SAED image (inset) of a single microbelt with a zone axis along [001]. (g) Absorption and PL spectra of the $FAPbBr_3$ MMB arrays.

2.5. Characterizations of the MHPs. X-ray diffraction (XRD) patterns were obtained by utilizing a Bruker D8 Advance X-ray diffractometer equipped with a Cu tube (λ = 1.5406 Å) operated at 40 kV and 20 mA. The UV−vis absorbance spectrum was measured by employing a Hitachi U4100 UV−vis−NIR spectrophotometer. Steady-state photoluminescence (PL) and time-resolved photoluminescence (TRPL) measurements were conducted using an FLS920 (Edinburgh Instruments) fluorescence spectrometer with a 275 nm excitation wavelength. The thicknesses of the MMBs were determined by utilizing a stylus profiler (Bruker, DektakXT). The roughness was determined by using an MFP-3D atomic force microscope.

2.6. Fabrication of Patterned Arrays-Based Flexible PDs. PDs were fabricated by depositing interdigital electrodes (Bi/Ag or Au electrode: 15/150 nm in thickness) onto the MMBs via vacuum evaporation using the metal mask. The gap between the two electrodes is about 20 μm.

2.7. Photodetection Performance Measurements. The $I-V$ characteristics were assessed by utilizing the Keithley 4200 semiconductor characterization system in both dark and illuminated environments. The $I-t$ curves were captured by connecting a Stanford SRS current preamplifier (SR570) and a Stanford SRS function generator (DS345). To evaluate the device's response and recovery speed, the temporal response was measured using a Mixed Domain Oscilloscope (Tektronix, MDO3104). The pulsed laser beams were generated by periodically switching the laser using the transistor−transistor logic (TTL) potential. The light source employed in this study was a 532 nm laser manufactured by Changchun New Industries Optoelectronics Technology Co., Ltd. The light power intensity was calibrated by utilizing a silicon photodiode (PM100D). Throughout the measurements, all devices remained unencapsulated and were stored in an ambient atmosphere.

2.8. Calculation Methods. All of the DFT calculations were carried out with the Vienna Ab initio Simulation Package (VASP). The exchange−correlation functional adapted in this work is the Perdew−Burke−Ernzerhof (PBE) functional within the generalized gradient approximation (GGA) method. The core−valence interactions were described by the projected augmented wave (PAW) method. The energy cutoff for plane wave expansions was set to 400 eV, and the 2 × 2 × 1 Monkhorst−Pack grid k-points were used to sample the Brillouin zone integration.

3. RESULTS

This study involved the growth of three representative microscale 3D perovskite SCs, specifically $FAPbBr_3$, $MAPbBr_3$, and $MAPbCl_3$, on Si/SiO_2 or glass substrates for the purpose of fabricating IPPE-based PDs. The monocrystalline microbelt

https://doi.org/10.1021/acsami.4c00302
ACS Appl. Mater. Interfaces 2024, 16, 16482−16493

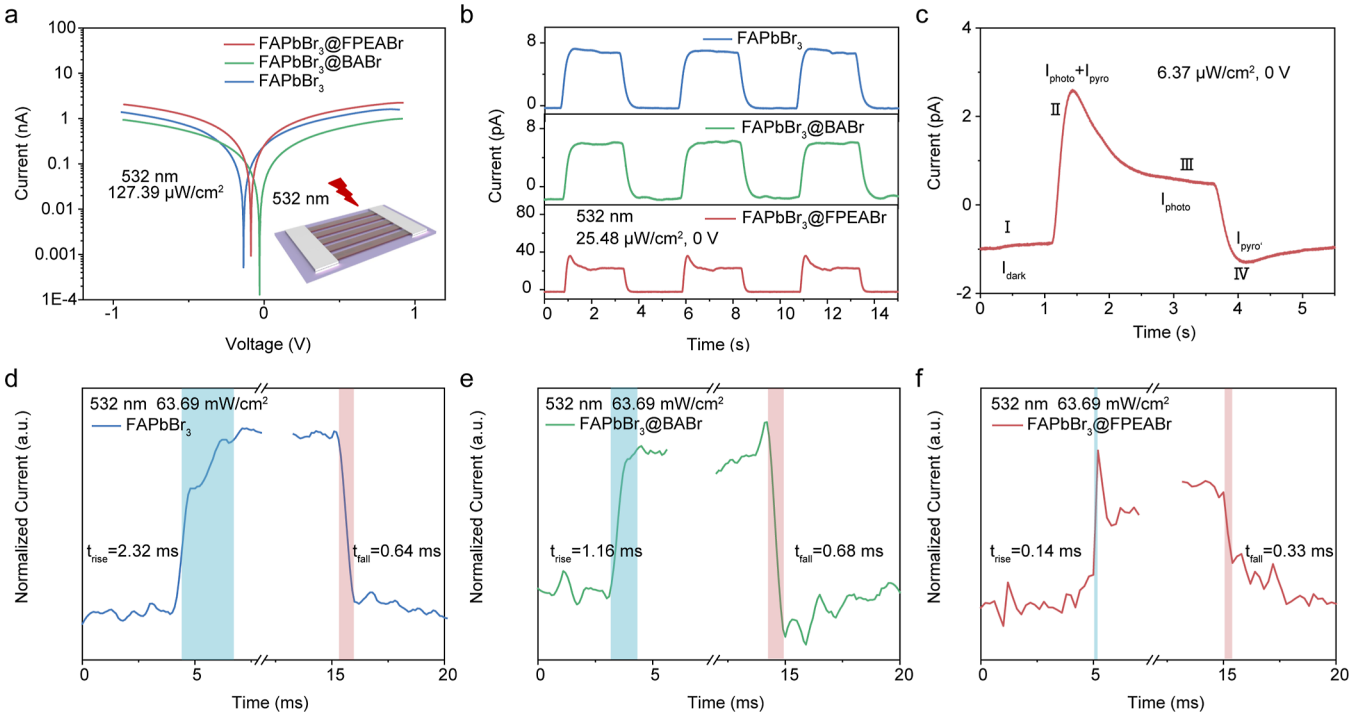

Figure 2. Comparison of performance of PDs based on $FAPbBr_3$ MMB arrays passivated with three different ammonium ligands. (a) *I*−*V* curves of three PDs under 532 laser illumination conditions with a power density of 127.4 μW cm^{-2}. Inset: schematic illustration of the $FAPbBr_3$ MMB array-based PDs. (b) Time-dependent photoresponses and (d−f) temporal responses of three PDs under 532 nm laser illumination and zero bias conditions, from which one can see that only $FAPbBr_3$@FPEABr one demonstrates the pyroelectric responses. (c) An enlarged view of the *I*−*t* curves of $FAPbBr_3$@FPEABr-based PD, showing a typical four-stage photoresponse behavior.

(MMB) arrays of $FAPbBr_3$ and $MAPbBr_3$ were prepared using a polydimethylsiloxane (PDMS) template-assisted[38,39] cosolvent evaporation crystallization technique[40] (Figure 1a). For $MAPbCl_3$, monocrystalline films (MFs) were obtained by a typical space-confined inverse temperature crystallization.[41] The Experimental Section provides a comprehensive account of the growth procedures. The objective of growing MHP SCs with varying components and morphologies is to establish the applicability of our surface passivation enhanced IPPE strategy in facilitating self-powered photodetection based on MHP SCs. The PDMS templates featuring periodic microchannels were acquired through the application of the PDMS prepolymer onto the previously prepared SU-8 patterned rectangular arrays. The optical images of the SU-8 microarrays can be observed in Figure S1a. The dimensions of SU-8 microarrays dictate the dimensions of the PDMS microchannels, thereby regulating the dimensions of the MMBs. The dimensions of the SU-8 microarrays in question are 1 μm in height and 20 μm in width. Once the microchannels were brought into contact with the substrate, they effectively restricted the movement of the solution, consequently confining the growth of the SC arrays. As the solvent DMF gradually evaporates, the solution becomes excessively concentrated, leading to a crystallization process taking place within the microchannels. Following thorough evaporation of the solvent, the PDMS template was carefully removed from the substrate, resulting in the presence of highly aligned MMBs on the substrate. Figure 1b,c depicts the top-view and cross-sectional scanning electron microscopy (SEM) images of the $FAPbBr_3$ MMB arrays. The microbelts exhibit a monocrystalline nature, characterized by smooth surfaces devoid of grain boundaries and surface defects. The cross-sectional analysis reveals a rectangular shape with an average thickness of 760 nm (Figure S1b). Also, atomic force microscopy (AFM) was conducted to determine the surface roughness of the $FAPbBr_3$ MMB arrays (Figure S2). A mean roughness of less than 2 nm was determined, indicating the smooth nature of the perovskite. The X-ray diffraction (XRD) patterns in Figure 1d revealed the high crystallinity and pristine crystallographic orientation of the MMBs, as evidenced by the presence of distinct characteristic peaks for the (001) and (011) crystallographic planes. The determination of the growth direction of the microbelt along [011] can be inferred from the low-magnification transmission electron microscopy (TEM) image in Figure 1e and the high-resolution TEM (HRTEM) image in Figure 1f. Additionally, the presence of smooth surfaces and distinct sharp edges can be observed in perovskite microbelts. Figure 1g illustrates the absorption spectrum of $FAPbBr_3$ MMBs, revealing a conspicuous band edge cutoff at approximately 575 nm devoid of any excitonic signature. This observation implies a limited presence of in-gap defect states. The optical bandgap of $FAPbBr_3$ MMBs can be ascertained as 2.17 eV through the utilization of the Tauc plot. Additionally, the $FAPbBr_3$ MMBs demonstrate photoluminescence (PL), with peak emission occurring at approximately 580 nm. The asymmetrical PL morphology may be attributed to the deviation of the molar ratio of FABr to $PbBr_2$ in the precursor solution.[42] The aforementioned characteristics collectively demonstrate the exceptional quality and singular crystal structure of the resulting $FAPbBr_3$ MMBs. For $MAPbBr_3$ MMBs and $MAPbCl_3$ MFs, the characterization results for both MHPs are presented in Figures S3 and S4, respectively. It has been demonstrated that both MHPs exhibit high crystallinity and smooth surfaces. The XRD patterns of $MAPbBr_3$ MMBs and $MAPbCl_3$ MFs

https://doi.org/10.1021/acsami.4c00302
ACS Appl. Mater. Interfaces 2024, 16, 16482−16493

indicate their single-crystalline nature, as evidenced by the presence of only (100), (200), and (300) diffraction peaks. These peaks correspond to the exposed crystal faces of (100). The bandgap values are determined to be 2.18 eV for $MAPbBr_3$ and 2.99 eV for $MAPbCl_3$.

Subsequently, as shown in Figure 2a, PDs employing Schottky-contacts with a lateral configuration were manufactured through the thermal evaporation of a pair of Bi/Ag electrodes onto the MMBs or MF. The choice of Bi as the electrode material was made to circumvent the potential concern of perovskite corrosion.[43] Ideal Schottky junctions are challenging to obtain in perovskite-based PDs fabricated through thermal evaporation for two main reasons. First, the incomplete volatilization of the solvent can introduce defects such as dangling bonds, nonperovskite phases, and residual precursor species onto the surfaces of the semiconductors, leading to a pinning effect.[32] Second, the chemical bonding between the metal and the semiconductor, along with their interdiffusion, has the potential to induce significant strain in the crystal lattices of both materials, consequently altering the band structures and the resulting Schottky barrier height (SBH).[44] Based on our preliminary findings, it is feasible to attain relatively optimal IPPE-based PDs by employing chemically polishing techniques on the SCs.[30] However, achieving a chemically polished surface for micro- or nanoscale MHP SCs poses significant challenges. In order to address this challenge, we endeavored to implement the passivation strategy as a means of regulating the band bending occurring at the interface between the metal and MHP. Therefore, prior to electrode deposition, the SCs underwent an initial cleaning process utilizing a solvent mixture comprising cyclohexane and *tert*-amyl alcohol (Figure S5a−c). Subsequently, the SCs were passivated by using various ammonium ligands. The comprehensive methodology is elucidated in the Experimental Section, wherein six ammonium ligands with diverse tail groups and alkyl chain lengths are chosen, as depicted in Figure S5d. The ammonium ligands used here are formamidine (FA), butylammonium (BA), and oleylamine (OA), which exhibit a chain structure, whereas phenethylammonium (PEA), 4-FPEA, and 3,4,5-trifluoroanilinium (345-FAn) possess benzene rings. According to the optical image presented in Figure S6, the distance between the two electrodes was 20 μm. In order to maintain uniformity in the effective area across various devices, only 40 MMBs were retained. Consequently, the effective illumination area can be estimated to be approximately 8×10^{-4} cm^2. We have chosen three representative devices, which are based on bare $FAPbBr_3$, $FAPbBr_3$ passivated with BABr, and $FAPbBr_3$ passivated with 4-FPEABr. These devices are denoted as $FAPbBr_3$, $FAPbBr_3$@BABr, and $FAPbBr_3$@FPEABr, respectively. Figure S7 presents a comparison of the dark current−voltage characteristic (I−V curves) for the three aforementioned devices. Due to the utilization of the same electrode pair, it is not possible to ascertain the explicit current rectification ratio. However, it is noteworthy that the $FAPbBr_3$@BABr-based PD exhibits the highest dark current, while the $FAPbBr_3$@FPEABr-based PD displays the lowest dark current. The identical outcomes can also be observed in the dark current and curve noise current at zero bias, as depicted in Figure S8, with the $FAPbBr_3$@FPEABr one demonstrating the minimal noise fluctuations. In this context, the noise currents of the PDs were ascertained by means of a Fourier transform analysis of the dark currents.[45] Also, one can see that the noise current is related to the frequency, demonstrating that the noise of the PD is dominated by the $1/f$ noise. In contrast to the dark I−V curves, the I−V curves obtained under 532 nm laser illumination depicted in Figure 2a reveal that the $FAPbBr_3$@FPEABr-based PD exhibits a greater photocurrent and a more pronounced rectification ratio. In the case of $FAPbBr_3$@BABr-based PDs, the presence of the smallest photocurrent and the weakest evident rectification characteristics can be observed. In addition, the light on/off photoresponses of the aforementioned three PDs were measured and graphed in Figure 2b while being subjected to 532 nm illumination at zero bias. Weak photoresponses without pyroelectric current peaks were observed in $FAPbBr_3$ and $FAPbBr_3$@BABr-based PDs. In the case of $FAPbBr_3$@FPEABr-based PDs, a discernible positive pyroelectric current is produced, resulting in a significant 10-fold amplification of the output currents compared to the counterparts. However, the negative pyroelectric photoresponses exhibit a weak magnitude. These phenomena have also been observed in other pyroelectric effect-based PDs.[46−48] In this study, a 532 nm laser was employed as the main light source since it has been observed that $FAPbBr_3$-based PDs exhibit the most significant photoresponses when stimulated by this particular wavelength (Figure S9). An enlarged cycle of on−off response of $FAPbBr_3$@FPEABr-based PDs is shown in Figure 2c, in which a typical four-stage photoresponse response behavior (I, dark current; II, positive pyroelectric current + photocurrent plateau; III, photocurrent plateau; IV, negative pyroelectric current) can be observed. After optical excitation, hot carriers are generated, followed by thermalization and relaxation. The positive pyroelectric currents are induced by a lattice temperature rise, while the photocurrents are derived from the collection of cooled photogenerated carriers. Furthermore, the introduction of passivation using 4-FPEABr significantly reduces the response time of PDs from 2.32 to 0.14 ms. Conversely, the response time and recovery time of $FAPbBr_3$@BABr-based PDs remain relatively unchanged. Given the limited absorption of 1064 nm photons by $FAPbBr_3$ SCs, a 1064 nm laser was employed as the heating method to validate the presence of IPPE. As depicted in Figure S9b, the PDs based on $FAPbBr_3$@FPEABr exhibit distinct photoresponses to the 785 nm laser, which exceeds the absorption limit of $FAPbBr_3$. Conversely, $FAPbBr_3$-based PDs exhibit no photoresponses toward the 785 nm laser. The aforementioned findings collectively demonstrate the significance of surface passivation in boosting the IPPE for self-powered PDs that rely on MHP SCs. Figure S10 illustrates the comprehensive self-powered performance of the $FAPbBr_3$@FPEABr/Bi/Ag Schottky junction-based PD in response to a 532 nm laser. The output currents are notably augmented by the pyroelectric effect, exhibiting a maximum enhancement of approximately 3.5 times compared to the plateau of photocurrent (Figure S10c). However, the negative pyroelectric current peaks of the PD are not prominent, especially when increasing power densities. This phenomenon is also seen in other pyro-phototronic effect-based PDs, which may be explained by the nonideal interfacial contact between perovskite and metal.[30] The charge carriers tend to transmit directly across the leaky Schottky barrier instead of the external circuit. The highest values for responsivity (R) and detectivity (D^*) are achieved at 0.3 A/W and 1×10^{10} Jones, respectively, under the lowest intensity of 0.13 $\mu W/cm^2$. In this study, the R and D^* were calculated and visually represented as a function of power

https://doi.org/10.1021/acsami.4c00302
ACS Appl. Mater. Interfaces 2024, 16, 16482−16493

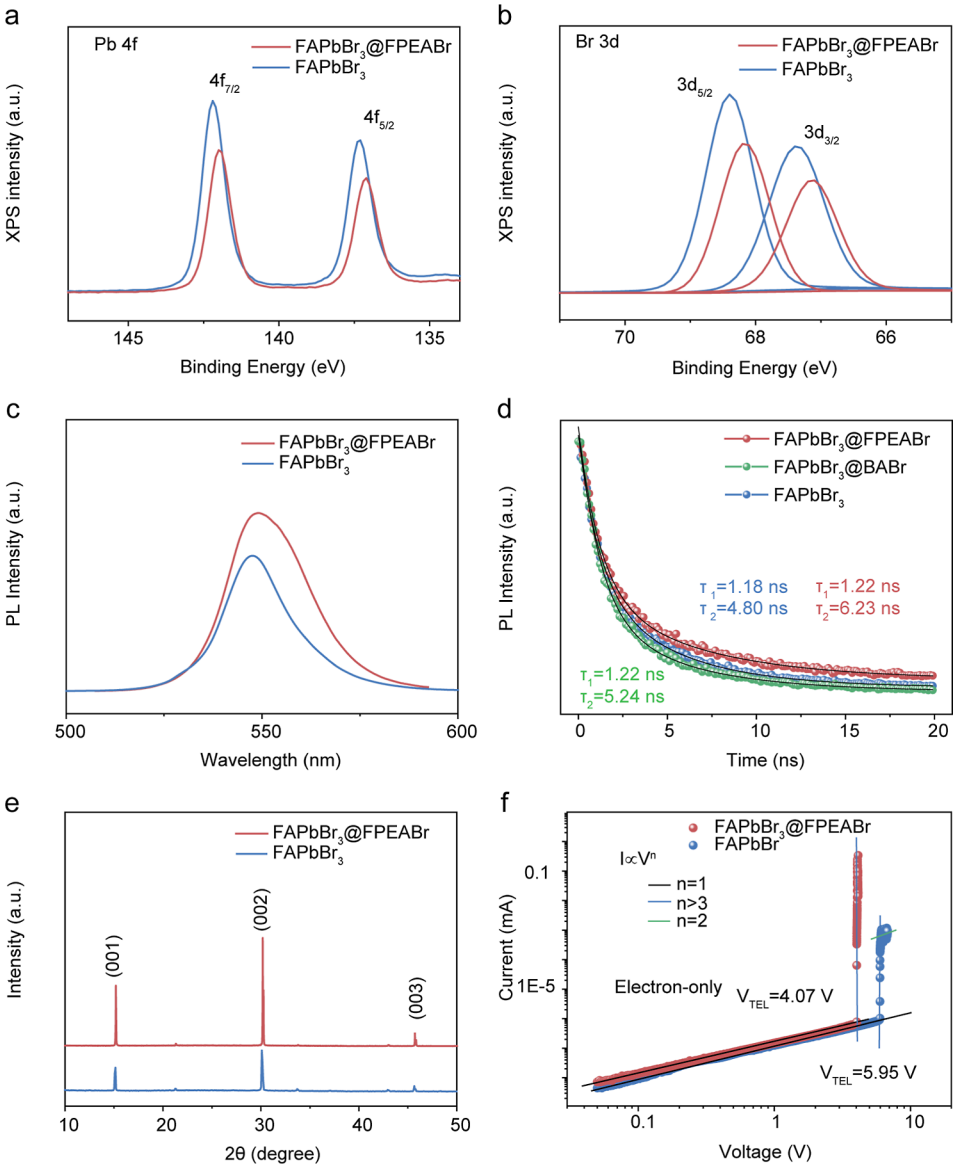

Figure 3. Passivation effect of 4-FPEABr on $FAPbBr_3$ MMB arrays. XPS spectra of (a) Pb 4f and (b) Br 3d for $FAPbBr_3$ and $FAPbBr_3$@FPEABr MMBs. (c) Steady-state, (d) time-resolved PL spectra, and (e) XRD patterns of $FAPbBr_3$ and $FAPbBr_3$@FPEABr MMBs. (f) Dark $I-V$ curves of the electron-only devices based on $FAPbBr_3$ and $FAPbBr_3$@FPEABr MMBs.

density, employing the equations provided in the following section

$$R = \frac{(I_{photo} - I_d)/S}{P} \quad (1)$$

$$D^* = \frac{(BS)^{1/2}}{NEP} = \frac{R_\lambda (BS)^{1/2}}{\overline{i_n^2}^{1/2}} \quad (2)$$

where I_{photo} is the photocurrent, I_d is the dark current, S is the active area, P is the light power density, B is the bandwidth, NEP is the noise equivalent power, and $\overline{i_n^2}^{1/2}$ is the root-mean-square value of the noise current. Furthermore, Figures S11 and S12 provide a comprehensive summary of the performances of PDs based on $FAPbBr_3$@BABr and $FAPbBr_3$. It is worth noting that no peak currents associated with pyroelectric currents were observed across all power densities. The $FAPbBr_3$@BABr-based PDs achieved a peak R of 0.22 A/W, while the $FAPbBr_3$-based PDs achieved a peak R of 6.2 mA/W, both of which are lower than those of the $FAPbBr_3$@FPEABr-based PDs. Further, we made a comparison of the present PDs with other previously reported perovskite-based self-powered PDs and other pyro-phototronic effect-based PDs in Table S1, from which one can see that our PDs demonstrate a good level of photoresponsivity and detectivity. From the statistical performances from ten devices plotted in Figure S13, one can see that better performances are obtained for $FAPbBr_3$@FPEABr-based PDs than the bare ones. Furthermore, we conducted an assessment on the impact of bias voltage on the photoresponses of $FAPbBr_3$@FPEABr-based PDs (Figure S14). It is observed that as the bias voltage increases, there is a tendency for the ratio of $R_{pyro+photo}/R_{photo}$ to increase rather than decrease. When the bias reaches 1.6 V, the pyroelectric currents vanish. These findings align with the outcomes reported in our previous publication.[30] For the pyroelectric current, the voltage has two opposite effects. On the one hand, the joule heat induced by the bias can hinder the change of the

https://doi.org/10.1021/acsami.4c00302
ACS Appl. Mater. Interfaces 2024, 16, 16482−16493

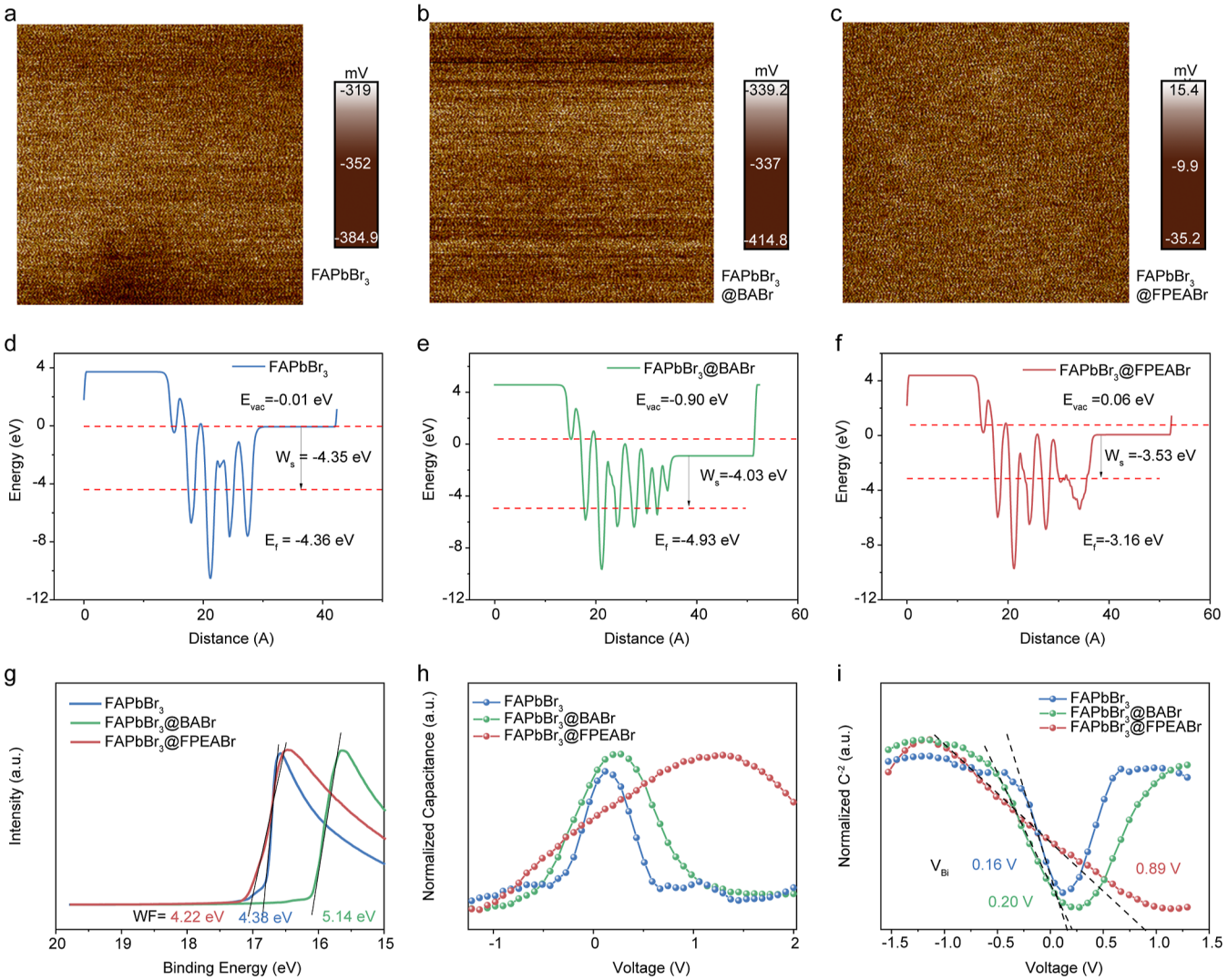

Figure 4. Energy level and built-in-field modulated by passivation with different ammonium ligands. KPFM images of the (a) $FAPbBr_3$, (b) $FAPbBr_3$@BABr, and (c) $FAPbBr_3$@FPEABr MMB arrays. The calculated work functions of the (d) $FAPbBr_3$, (e) $FAPbBr_3$@BABr, and (f) $FAPbBr_3$@FPEABr MMB arrays. (g) High binding energy cut-offs of the UPS spectra of the $FAPbBr_3$, $FAPbBr_3$@BABr, and $FAPbBr_3$@FPEABr MMB arrays. (h) Capacitance−voltage curves of $FAPbBr_3$, $FAPbBr_3$@BABr, and $FAPbBr_3$@FPEABr MMB arrays/Bi Schottky junctions. (i) C^{-2} obtained from (h) as a function of bias voltage (Mott−Schottky curves), showing different V_{Bi}.

polarization, impairing the pyro-phototronic-effect. On the other hand, moderate voltage is beneficial for band bending, which is the origin of interfacial the pyro-phototronic-effect. Therefore, the pyroelectric current changed obviously with changing positive and negative voltage. The photoresponses induced by IPPE typically relied on the temperature increases resulting from the generation and thermalization of hot carriers.[49] Hence, an infrared camera was employed to record the real-time fluctuations in temperature. The thermal images depicted in Figure S15 show that the laser irradiation of the $FAPbBr_3$ MMBs resulted in a noticeable elevation in temperature when contrasted with the absence of light. Additionally, as the laser power density escalated, the extent of the temperature increase induced by light also exhibited a substantial augmentation. Furthermore, Figure S16 demonstrates that the most pronounced alterations in temperature were observed for 532 nm. The temperate rise by light illumination is generated by a hot carrier relaxation procedure. In real situations, the temperature is influenced by light absorption and light energy. From the absorption spectrum in Figure 1g, one can see that 532 nm is close to the absorption cutoff wavelength of $FAPbBr_3$. For lasers with shorter wavelengths, although the hot carriers are generated with their energies above the bandgap, the penetration depths are insufficient. For lasers with longer wavelengths, they cannot be effectively absorbed by perovskite. Therefore, a balance between light energy and penetration depth is needed. A laser with a wavelength slightly smaller than the absorption cutoff wavelength usually causes the highest temperature rise, which is also confirmed in our early reports.[30,43] The similar PDs were then fabricated using the Schottky structure of perovskite/Bi/Ag, with $FAPbBr_3$@FA, $FAPbBr_3$@OA, $FAPbBr_3$@PEA, and $FAPbBr_3$@345FAN as the materials of interest. The $I-t$ curves under zero bias for the above four PDs are depicted in Figure S17, with illumination provided by a 532 nm laser. No obvious pyroelectric currents are observed in $FAPbBr_3$ passivated by an ammonium ligand lacking a benzene ring. Conversely, $FAPbBr_3$ passivated by an ammonium ligand containing a benzene ring displays four-stage photoresponse behaviors in all $I-t$ curves. These findings provide conclusive

https://doi.org/10.1021/acsami.4c00302
ACS Appl. Mater. Interfaces 2024, 16, 16482−16493

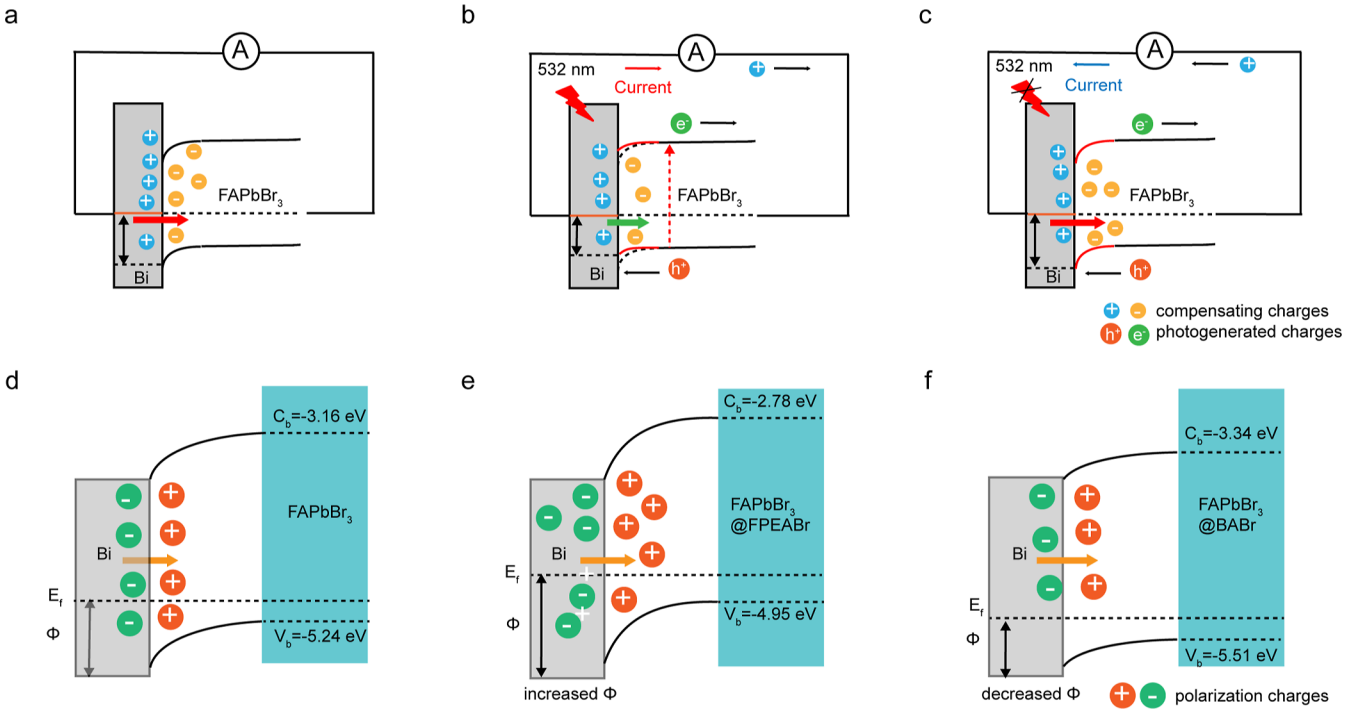

Figure 5. Mechanisms of the interfacial pyro-phototronic effect modulated by surface passivation. Schematic energy band diagrams of the $FAPbBr_3$ MMB/Bi Schottky contact at (a) equilibrium state and the moment of (b) light on and (c) light off. Illustration of the band bending and the resultant interfacial polarization at the Schottky junction interface based on (d) $FAPbBr_3$, (e) $FAPbBr_3$@FPEABr, and (f) $FAPbBr_3$@BABr MMB arrays.

evidence that the utilization of the ammonium ligands with specific functional groups for surface passivation can significantly regulate the IPPE, thereby improving the performance of MHP SCs based on PDs. In order to provide additional evidence of the universality of our strategy, we also fabricated PDs based on the $FAPbBr_3$@FPEA/Au Schottky contact, $MAPbBr_3$@FPEA/Bi Schottky contact, and $MAPbCl_3$@FPEA/Bi Schottky contact. The $I-t$ curves of photodetectors PDs based on the aforementioned three structures are illustrated in Figures S18−S20. All of these structures demonstrate photoresponse behaviors induced by interfacial polarization and exhibit higher output currents compared to the nonpassivated PDs. Notably, $MAPbCl_3$@FPEA/Bi PDs display significant positive and negative pyroelectric currents, with $I_{pyro+photo}$ being considerably higher than I_{photo}. This phenomenon may be due to the higher V_{Bi} in $MAPbCl_3$-based devices since $MAPbCl_3$ has a higher energy level.

Further characterizations were conducted to thoroughly investigate the underlying mechanism of the modulating effect of surface passivation on IPPE. Similar to the traditional surface passivation, the passivation with 4-FPEABr can significantly improve the quality of the MMBs. The interaction between Pb^{2+} and 4-FPEABr was confirmed through X-ray photoelectron spectroscopy (XPS), as evidenced by the observed shift in the Pb 4f peak, as depicted in Figure 3a. The reduction in Pb^{2+} binding energy can be attributed to the ability of F-PEA to diminish the electron cloud density surrounding Pb^{2+}.[50] Furthermore, the peaks of Br also shifted to a lower binding energy. It is noteworthy that the 4-FPEABr compound exhibited a significant enhancement in the steady-state PL intensity, as depicted in Figure 3c. Additionally, the photoluminescence lifetimes associated with surface recombination and bulk recombination displayed an increase, as shown in Figure 3d, suggesting a reduction in the number of nonradiative recombination defects through passivation. Conversely, in the case of $FAPbBr_3$@BA, there was a slight decrease in the observed lifetimes. The XRD patterns and trap densities for electrons provide evidence of enhanced crystallinity in $FAPbBr_3$@FPEA. Analysis of Figure 3e reveals the absence of any new phases and a substantial increase in the peak intensity. Furthermore, it can be inferred that the passivators do not give rise to a two-dimensional perovskite structure on the $FAPbBr_3$. The trap densities can be computed using the following equation

$$n_{trap} = \frac{2\varepsilon_0\varepsilon_r V_{TFL}}{eL^2} \quad (3)$$

where ε_0 is the vacuum permittivity, ε_r is the relative dielectric constant, V_{TFL} is the trap-filled limit voltage, e is the electron charge, and L is the gap distance. Furthermore, the implementation of 4-FPEABr passivation resulted in a significant decrease in V_{TFL}, reducing it from 5.95 to 4.07 V. Moreover, the surface passivation can greatly improve the long-term stability toward humidity and thermal treatments (Figure S21).

Although the aforementioned findings collectively suggest that the incorporation of 4-FPEABr enhances the overall quality of the $FAPbBr_3$ MMBs, they are not sufficient to explain the IPPE induced by 4-FPEABr passivation. The interfacial pyroelectric effect arises from the interfacial polarization caused by energy band bending at the surface between MHPs and metals. Therefore, the underlying mechanisms can be elucidated by considering the WF induced by passivation with various ammonium ligands. First, KPFM was utilized to validate the surface potential distributions in

https://doi.org/10.1021/acsami.4c00302
ACS Appl. Mater. Interfaces 2024, 16, 16482−16493

$FAPbBr_3$, $FAPbBr_3$@BA, and $FAPbBr_3$@FPEABr MMBs (Figure 4a–c). The uniform KPFM images indicate the homogeneous surface of three MMBs. The MMBs with bare, BABr-, and 4-FPEABr passivation exhibited contact potential difference (CPD) values of −352, −377, and −9.9 meV, respectively. The CPD value for $FAPbBr_3$@FPEABr MMBs was significantly higher than that of the pristine MMB, while BABr slightly reduced the CPD. The higher positive CPD value observed for the $FAPbBr_3$@FPEABr MMB suggests a correspondingly lower surface WF value, whereas the presence of BABr leads to an increase in the surface WF value. Similar results were also proven by solid-state DFT calculations (Figures 4d–f and S22). The alteration in WF resulting from surface passivation is clearly demonstrated through UPS (Figure 4g). By examining the high binding energy cutoff regions of the three MMBs, the actual WF values can be computed as 4.22 eV for $FAPbBr_3$@FPEABr, 4.38 eV for $FAPbBr_3$, and 5.14 eV for $FAPbBr_3$@BABr. The observed trend in the WF values aligns with the findings obtained from KPFM and computational analysis. Subsequently, the electrical characteristics of three PDs in the absence of light were ascertained through Mott–Schottky analysis, employing the measurement of C–V curves (Figure 4h,i). By conducting linear regression on $C(V)^{-2}$ against the bias voltage (the Mott–Schottky curve), a V_{bi} of 0.89 V was determined for $FAPbBr_3$@FPEABr, surpassing the values of 0.2 V for $FAPbBr_3$ and 0.16 V for $FAPbBr_3$@BA. Hence, the PDs utilizing $FAPbBr_3$@FPEABr MMBs exhibit notably enhanced photoresponses induced by IPPE in comparison to the remaining two devices.

The energy band diagrams presented in Figure 5a–c provide clarification on the phenomenon of IPPE. The structure of our device is a back-to-back contacted Schottky junction. Since the two electrodes were thermally evaporated onto the perovskite SCs and the surfaces of the SCs were not ideal, the two back-to-back contacted Schottky barriers are not the same, leading to the asymmetric geometry of the structures. Although the same metals were used for device fabrication, when connected in an external circuit, it is not possible to create two barriers at the same time. For two electrodes, one is in a positive connection, and another is in a reversed connection. In the equilibrium state (Figure 5a), a Schottky junction forms at the interface between p-type $FAPbBr_3$ and Bi. The depletion layer at this interface acts as a thin layer of electric polarization, with positive polar charges located on the $FAPbBr_3$ side and negative charges on the metal side. The polarization direction is oriented from Bi toward $FAPbBr_3$. To preserve the electric neutrality of the device, the holes present in the metal and the electrons in $FAPbBr_3$ serve as compensating charges. The Schottky junction functions as a barrier to impede the recombination of these compensating charges. Due to the temperature-dependent electrical properties and built-in field exhibited by MHPs, alterations in temperature will result in variations in the intensity of interfacial polarization. Consequently, the modulation of temperature through light on/off transitions will give rise to positive or negative pyroelectric currents. As a result, the IPPE is significantly influenced by both the barrier height and the V_{Bi}. The modulation of the WF of the perovskite surface through passivation with various ammonium ligands can result in changes to the band structure between MHPs and metals. Consequently, the occurrence of band bending at different levels can be anticipated. Based on the observed low binding energy cutoffs of the UPS spectra (Figure S23a) and the determined WF values of the three $FAPbBr_3$ MMBs, it is possible to deduce the corresponding energy levels, as depicted in Figure S23b. The WF values of $FAPbBr_3$@FPEABr, $FAPbBr_3$@BABr, and $FAPbBr_3$ allow for the construction of the corresponding band diagrams. Figure 5d illustrates that under equilibrium conditions, $FAPbBr_3$ exhibits a moderate downward bending at the interfaces between the perovskite surface and Bi. However, the relatively small SBH fails to adequately sustain interfacial polarization, leading to negligible pyroelectric properties. The $FAPbBr_3$@FPEABr system gives rise to a space charge region at the interface between $FAPbBr_3$ and Bi, leading to increased downward bending (Figure 5e). This enhanced bending strengthens the effective barrier, built-in field, and resulting V_{Bi}. The presence of this effective barrier, V_{Bi}, is crucial for the manifestation of pyroelectric properties in the junction. Therefore, the $FAPbBr_3$@FPEABr MMBs-based PDs demonstrate the IPPE-based photoresponses and the highest performances. However, in the case of $FAPbBr_3$@BABr, the presence of a significantly less effective barrier will facilitate the redistribution of charge carriers through direct electron transmission across the interface, achieved through either tunneling or thermionic emission (Figure 5f).[28] In this case, the pyroelectric effect will be severely damaged.

4. CONCLUSIONS

In conclusion, a practical and widely applicable approach for enhancing the interface passivation of MHP SCs has been demonstrated. This approach enables the development of self-powered PDs utilizing Schottky junctions by manipulating the surface band structure between the MHP and metals. The utilization of ammonium ligands with a benzene ring for passivation purposes not only effectively mitigates surface defects but also induces a decrease in the WF values. Consequently, this passivation-assisted band bending phenomenon generates IPPE at the interface, resulting in improved photodetection performance and an expanded spectral range of response for MHP SCs based on Schottky junctions. This strategy offers a viable and efficient approach to generate interfacial pyroelectricity in MHPs, thereby enabling its potential utilization in practical applications, including energy conversion and infrared sensors.

■ ASSOCIATED CONTENT

Supporting Information

The Supporting Information is available free of charge at https://pubs.acs.org/doi/10.1021/acsami.4c00302.

Experimental section of the whole process, photographs, SEM images, XRD patterns, PL spectra, absorbance spectra, thermograms, UPS spectra of perovskite single crystals, statistical performances, energy band diagrams, temporal response, photoresponse spectra, I–V characteristics, I–t characteristics, dark currents, and stability of devices (PDF)

■ AUTHOR INFORMATION

Corresponding Authors

Xingyuan San − *Hebei Key Laboratory of Photo-Electricity Information and Materials, National & Local Joint Engineering Laboratory of New Energy Photoelectric Devices, College of Physics Science and Technology, Hebei University, Baoding 071002, P. R. China*; Email: xysan@hbu.edu.cn

https://doi.org/10.1021/acsami.4c00302
ACS Appl. Mater. Interfaces 2024, 16, 16482−16493

Caofeng Pan − *Institute of Atomic Manufacturing, Beihang University, Beijing 100191, P. R. China;* orcid.org/0000-0001-6327-9692; Email: pancaofeng@buaa.edu.cn

Zheng Yang − *Hebei Key Laboratory of Photo-Electricity Information and Materials, National & Local Joint Engineering Laboratory of New Energy Photoelectric Devices, College of Physics Science and Technology, Hebei University, Baoding 071002, P. R. China; Institute of Life Science and Green Development, Hebei University, Baoding 071002, P. R. China;* orcid.org/0000-0001-7172-4717; Email: yangzheng06@hbu.edu.cn

Authors

Linjuan Guo − *Hebei Key Laboratory of Photo-Electricity Information and Materials, National & Local Joint Engineering Laboratory of New Energy Photoelectric Devices, College of Physics Science and Technology, Hebei University, Baoding 071002, P. R. China*

Yi Song − *Hebei Key Laboratory of Photo-Electricity Information and Materials, National & Local Joint Engineering Laboratory of New Energy Photoelectric Devices, College of Physics Science and Technology, Hebei University, Baoding 071002, P. R. China*

Baorong Wang − *Hebei Key Laboratory of Photo-Electricity Information and Materials, National & Local Joint Engineering Laboratory of New Energy Photoelectric Devices, College of Physics Science and Technology, Hebei University, Baoding 071002, P. R. China*

Ridong Cong − *Hebei Key Laboratory of Photo-Electricity Information and Materials, National & Local Joint Engineering Laboratory of New Energy Photoelectric Devices, College of Physics Science and Technology, Hebei University, Baoding 071002, P. R. China*

Lei Zhao − *Hebei Key Laboratory of Photo-Electricity Information and Materials, National & Local Joint Engineering Laboratory of New Energy Photoelectric Devices, College of Physics Science and Technology, Hebei University, Baoding 071002, P. R. China;* orcid.org/0000-0001-9226-2929

Suheng Zhang − *Hebei Key Laboratory of Photo-Electricity Information and Materials, National & Local Joint Engineering Laboratory of New Energy Photoelectric Devices, College of Physics Science and Technology, Hebei University, Baoding 071002, P. R. China*

Leipeng Li − *Hebei Key Laboratory of Photo-Electricity Information and Materials, National & Local Joint Engineering Laboratory of New Energy Photoelectric Devices, College of Physics Science and Technology, Hebei University, Baoding 071002, P. R. China; Institute of Life Science and Green Development, Hebei University, Baoding 071002, P. R. China*

Wenqiang Wu − *Institute of Atomic Manufacturing, Beihang University, Beijing 100191, P. R. China*

Shufang Wang − *Hebei Key Laboratory of Photo-Electricity Information and Materials, National & Local Joint Engineering Laboratory of New Energy Photoelectric Devices, College of Physics Science and Technology, Hebei University, Baoding 071002, P. R. China*

Complete contact information is available at: https://pubs.acs.org/10.1021/acsami.4c00302

Author Contributions

L.G. and Y.S. contributed equally to this work. Z.Y. conceived and supervised the project. L.G. and Y.S. synthesized the perovskites and measured the optoelectronic properties. B.W. contributed to the AFM measurement. R.C. contributed to the fabrication of the devices. L.Z. contributed to the $C-V$ measurement. S.Z. and L.L. contributed to the steady PL measurement. W.W. contributed to the transient PL measurement. L.G. wrote the manuscript. Z.Y. and L.G. modified it. S.W. and C.P. provided funding support and critical suggestions for this work. All the authors reviewed the manuscript.

Notes

The authors declare no competing financial interest.

■ ACKNOWLEDGMENTS

This work was supported by the National Natural Science Foundation of China (grant nos. U20A20166, 62005072, and 62104057), the Natural Science Foundation of Hebei Province (grant no. E2021201016), the Hebei Education Department (grant no. BJK2022050), the Science and Technology Plan Project of Hebei Province (grant nos. 226Z1002G and 226Z1703G), and the Hebei Province Optoelectronic Information Materials Laboratory Performance Subsidy Fund Project (no. 22567634H).

■ REFERENCES

(1) Cao, F.; Hu, Z.; Yan, T.; Hong, E.; Deng, X.; Wu, L.; Fang, X. A Dual-Functional Perovskite-Based Photodetector and Memristor for Visual Memory. *Adv. Mater.* **2023**, *35*, 2304550.

(2) Feng, S.; Li, J.; Feng, L.; Liu, Z.; Wang, J.; Cui, C.; Zhou, O.; Deng, L.; Xu, H.; Leng, B.; Chen, X. Q.; Jiang, X.; Liu, B.; Zhang, X. Dual-mode Conversion of Photodetector And Neuromorphic Vision Sensor via Bias Voltage Regulation on A Single Device. *Adv. Mater.* **2023**, *35*, 2308090.

(3) Muhammad; Choi, D.; Parmar, D. H.; Rehl, B.; Zhang, Y.; Atan, O.; Kim, G.; Xia, P.; Pina, J. M.; Li, M.; Liu, Y.; Voznyy, O.; Hoogland, S.; Sargent, E. H. Halide-Driven Synthetic Control of InSb Colloidal Quantum Dots Enables Short-Wave Infrared Photodetectors. *Adv. Mater.* **2023**, *35*, 2306147.

(4) Liu, W.; Lv, J.; Peng, L.; Guo, H.; Liu, C.; Liu, Y.; Li, W.; Li, L.; Liu, L.; Wang, P.; Bodepudi, S. C.; Shehzad, K.; Hu, G.; Liu, K.; Sun, Z.; Hasan, T.; Xu, Y.; Wang, X.; Gao, C.; Yu, B.; Duan, X. Graphene Charge-Injection Photodetectors. *Nat. Electron.* **2022**, *5*, 281−288.

(5) Hu, X.; Li, X.; Li, G.; Ji, T.; Ai, F.; Wu, J.; Ha, E.; Hu, J. Recent Progress of Methods to Enhance Photovoltaic Effect for Self-Powered Heterojunction Photodetectors and Their Applications in Inorganic Low-Dimensional Structures. *Adv. Funct. Mater.* **2021**, *31*, 2011284.

(6) Cheng, W.; He, X.; Wang, J. G.; Tian, W.; Li, L. N -(2-aminoethyl) Acetamide Additive Enables Phase-Pure and Stable alpha-$FAPbI_3$ for Efficient Self-Powered Photodetectors. *Adv. Mater.* **2022**, *34*, 2208325.

(7) Ouyang, T.; Zhao, X.; Xun, X.; Gao, F.; Zhao, B.; Bi, S.; Li, Q.; Liao, Q.; Zhang, Y. Boosting Charge Utilization in Self-Powered Photodetector for Real-Time High-Throughput Ultraviolet Communication. *Adv. Sci.* **2023**, *10*, 2301585.

(8) Sun, Y.; Ge, L.; Dai, L.; Cho, C.; Ferrer Orri, J.; Ji, K.; Zelewski, S. J.; Liu, Y.; Mirabelli, A. J.; Zhang, Y.; Huang, J. Y.; Wang, Y.; Gong, K.; Lai, M. C.; Zhang, L.; Yang, D.; Lin, J.; Tennyson, E. M.; Ducati, C.; Stranks, S. D.; Cui, L. S.; Greenham, N. C. Bright and Stable Perovskite Light-Emitting Diodes in the Near-infrared Range. *Nature* **2023**, *615*, 830−835.

(9) Yang, Y.; Cheng, S.; Zhu, X.; Li, S.; Zheng, Z.; Zhao, K.; Ji, L.; Li, R.; Liu, Y.; Liu, C.; Lin, Q.; Yan, N.; Wang, Z. Inverted Perovskite Solar Cells With Over 2,000 h Operational Stability At 85 °C Using Fixed Charge Passivation. *Nat. Energy* **2024**, *9*, 37−46.

(10) Zhou, Y.; Fei, C.; Uddin, M. A.; Zhao, L.; Ni, Z.; Huang, J. Self-powered Perovskite Photon-counting Detectors. *Nature* **2023**, *616*, 712−718.
(11) Zhu, H.; Yang, W.; Reo, Y.; Zheng, G.; Bai, S.; Liu, A.; Noh, Y.-Y. Tin Perovskite Transistors and Complementary Circuits Based on A-site Cation Engineering. *Nat. Electron.* **2023**, *6*, 650−657.
(12) Li, S. X.; Xu, Y. S.; Li, C. L.; Guo, Q.; Wang, G.; Xia, H.; Fang, H. H.; Shen, L.; Sun, H. B. Perovskite Single-Crystal Microwire-Array Photodetectors with Performance Stability beyond 1 Year. *Adv. Mater.* **2020**, *32*, 2001998.
(13) Yang, Z.; Deng, Y.; Zhang, X.; Wang, S.; Chen, H.; Yang, S.; Khurgin, J.; Fang, N. X.; Zhang, X.; Ma, R. High-Performance Single-Crystalline Perovskite Thin-Film Photodetector. *Adv. Mater.* **2018**, *30*, 1704333.
(14) Feng, J.; Gong, C.; Gao, H.; Wen, W.; Gong, Y.; Jiang, X.; Zhang, B.; Wu, Y.; Wu, Y.; Fu, H.; Jiang, L.; Zhang, X. Single-crystalline Layered Metal-halide Perovskite Nanowires for Ultra-sensitive Photodetectors. *Nat. Electron.* **2018**, *1*, 404−410.
(15) Cao, F.; Meng, L.; Wang, M.; Tian, W.; Li, L. Gradient Energy Band Driven High-Performance Self-Powered Perovskite/CdS Photodetector. *Adv. Mater.* **2019**, *31*, 1806725.
(16) Min, L.; Tian, W.; Cao, F.; Guo, J.; Li, L. 2D Ruddlesden-Popper Perovskite with Ordered Phase Distribution for High-Performance Self-Powered Photodetectors. *Adv. Mater.* **2021**, *33*, 2101714.
(17) Han, B.; Liu, B.; Wang, G.; Qiu, Q.; Wang, Z.; Xi, Y.; Cui, Y.; Ma, S.; Xu, B.; Hsu, H. Y. Transparent and Reusable Nanostencil Lithography for Organic-Inorganic Hybrid Perovskite Nanodevices. *Adv. Funct. Mater.* **2023**, *33*, 2300570.
(18) Lai, Q.; Zhu, L.; Pang, Y.; Xu, L.; Chen, J.; Ren, Z.; Luo, J.; Wang, L.; Chen, L.; Han, K.; Lin, P.; Li, D.; Lin, S.; Chen, B.; Pan, C.; Wang, Z. L. Piezo-phototronic Effect Enhanced Photodetector Based on $CH_3NH_3PbI_3$ Single Crystals. *ACS Nano* **2018**, *12*, 10501−10508.
(19) Ding, R.; Lyu, Y.; Wu, Z.; Guo, F.; Io, W. F.; Pang, S. Y.; Zhao, Y.; Mao, J.; Wong, M. C.; Hao, J. Effective Piezo-Phototronic Enhancement of Flexible Photodetectors Based on 2D Hybrid Perovskite Ferroelectric Single-Crystalline Thin-Films. *Adv. Mater.* **2021**, *33*, 2101263.
(20) Yang, Z.; Jiang, M. M.; Guo, L. J.; Hu, G. F.; Gu, Y. S.; Xi, J. G.; Huo, Z. H.; Li, F. T.; Wang, S. F.; Pan, C. F. A High Performance $CsPbBr_3$ Microwire Based Photodetector Boosted by Coupling Plasmonic and Piezo-phototronic Effects. *Nano Energy* **2021**, *85*, 105951.
(21) Li, X.; Zhang, F.; Yue, Z.; Wang, Q.; Sun, Z.; Luo, J.; Liu, X. Centimeter-Size Single Crystals of Halide Perovskite Photoferroelectric Solid Solution with Ultrahigh Pyroelectricity Boosted Photodetection. *Angew. Chem., Int. Ed.* **2023**, *62*, 202305310.
(22) Tang, L.; Han, S.; Ma, Y.; Liu, Y.; Hua, L.; Xu, H.; Guo, W.; Wang, B.; Sun, Z.; Luo, J. Giant Near-Room-Temperature Pyroelectric Figures-of-Merit Originating from Unusual Dielectric Bistability of Two-Dimensional Perovskite Ferroelectric Crystals. *Chem. Mater.* **2022**, *34*, 8898−8904.
(23) Li, Z.; Ji, C.; Fan, Y.; Zhu, T.; You, S.; Wu, J.; Li, R.; Zhu, Z. K.; Yu, P.; Kuang, X.; Luo, J. Circularly Polarized Light-Dependent Pyro-Phototronic Effect from 2D Chiral-Polar Double Perovskites. *J. Am. Chem. Soc.* **2023**, *145*, 25134−25142.
(24) Guo, L. J.; Qi, Y. Q.; Yang, Z.; Zhao, L.; Zhang, W.; Wang, X. Z.; Liu, H. X.; Yan, G. Y.; Wang, S. F.; Pan, C. F. 2D Ruddlesden-Popper Perovskite Ferroelectric Film for High-performance, Self-powered and Ultra-stable UV Photodetector Boosted by Ferro-pyro-phototronic Effect and Surface Passivation. *Nano Energy* **2022**, *102*, 107714.
(25) Yang, Z.; Li, X. L.; Gao, L. J.; Zhang, W.; Wang, X. Z.; Liu, H. X.; Wang, S. F.; Pan, C. F.; Guo, L. J. Ferro-pyro-phototronic Effect Enhanced Self-powered, Flexible and Ultra-stable Photodetectors Based on Highly Crystalized 1D/3D Ferroelectric Perovskite Film. *Nano Energy* **2022**, *102*, 107743.
(26) Liu, Y.; Pan, X.; Liu, X.; Han, S.; Wang, J.; Lu, L.; Xu, H.; Sun, Z.; Luo, J. Tailoring Interlayered Spacers of Two-Dimensional Cesium-Based Perovskite Ferroelectrics toward Exceptional Ferro-Pyro-Phototronic Effects. *Small* **2022**, *18*, 2106888.
(27) Wan, J.; Yuan, H.; Xiao, Z.; Sun, J.; Peng, Y.; Zhang, D.; Yuan, X.; Zhang, J.; Li, Z.; Dai, G.; Yang, J. 2D Ruddlesden-Popper Polycrystalline PerovskitePyro-Phototronic Photodetectors. *Small* **2023**, *19*, 2207185.
(28) Yang, M. M.; Luo, Z. D.; Mi, Z.; Zhao, J.; E, S. P.; Alexe, M. Piezoelectric and Pyroelectric Effects Induced by Interface Polar Symmetry. *Nature* **2020**, *584*, 377−381.
(29) Ahmadi, R.; Abnavi, A.; Ghanbari, H.; Mohandes, H.; Mohammadzadeh, M. R.; De Silva, T.; Hasani, A.; Fawzy, M.; Kabir, F.; Adachi, M. M. Self-powered, Broadband, and Polarization-Sensitive Pyroelectric-Photoelectric Photodetector Based on Silicon-Water Heterojunction. *Nano Energy* **2022**, *98*, 107285.
(30) Guo, L. J.; Wang, H.; Xu, Z. Q.; Cong, R. D.; Zhao, L.; Zhang, S. H.; Zhang, K.; Gao, L. J.; Wang, S. F.; Pan, C. F.; Yang, Z. Interfacial Pyro-Phototronic Effect: A Universal Approach for Enhancement of Self-Powered Photodetection Based on Perovskites with Centrosymmetry. *Adv. Funct. Mater.* **2023**, *33*, 2306526.
(31) Zhang, H.; Pfeifer, L.; Zakeeruddin, S. M.; Chu, J.; Gratzel, M. Tailoring Passivators for Highly Efficient and Stable Perovskite Solar Cells. *Nat. Rev. Chem* **2023**, *7*, 632−652.
(32) She, X.-J.; Chen, C.; Divitini, G.; Zhao, B.; Li, Y.; Wang, J.; Orri, J. F.; Cui, L.; Xu, W.; Peng, J.; Wang, S.; Sadhanala, A.; Sirringhaus, H. A Solvent-based Surface Cleaning and Passivation Technique for Suppressing Ionic Defects in High-mobility Perovskite Field-Effect Transistors. *Nat. Electron.* **2020**, *3*, 694−703.
(33) Liu, C.; Yang, Y.; Chen, H.; Xu, J.; Liu, A.; Bati, A. S. R.; Zhu, H.; Grater, L.; Hadke, S. S.; Huang, C.; Sangwan, V. K.; Cai, T.; Shin, D.; Chen, L. X.; Hersam, M. C.; Mirkin, C. A.; Chen, B.; Kanatzidis, M. G.; Sargent, E. H. Bimolecularly Passivated Interface Enables Efficient and Stable Inverted Perovskite Solar Cells. *Science* **2023**, *382*, 810−815.
(34) Park, S. M.; Wei, M.; Xu, J.; Atapattu, H. R.; Eickemeyer, F. T.; Darabi, K.; Grater, L.; Yang, Y.; Liu, C.; Teale, S.; Chen, B.; Chen, H.; Wang, T.; Zeng, L.; Maxwell, A.; Wang, Z.; Rao, K. R.; Cai, Z.; Zakeeruddin, S. M.; Pham, J. T.; Risko, C. M.; Amassian, A.; Kanatzidis, M. G.; Graham, K. R.; Gratzel, M.; Sargent, E. H. Engineering Ligand Reactivity Enables High-temperature Operation of Stable Perovskite Solar Cells. *Science* **2023**, *381*, 209−215.
(35) Zhang, W.; He, L.; Meng, Y.; Kanda, H.; Tang, D.; Ding, B.; Ding, Y.; Nazeeruddin, M. K.; Li, X. Dual-Site Synergistic Passivation for Highly Efficient and Stable Perovskite Solar Cells. *Adv. Energy Mater.* **2022**, *12*, 2202189.
(36) Shirzadi, E.; Ansari, F.; Jinno, H.; Tian, S.; Ouellette, O.; Eickemeyer, F. T.; Carlsen, B.; Van Muyden, A.; Kanda, H.; Shibayama, N.; Tirani, F. F.; Grätzel, M.; Hagfeldt, A.; Nazeeruddin, M. K.; Dyson, P. J. High-Work-Function 2D Perovskites as Passivation Agents in Perovskite Solar Cells. *ACS Energy Lett.* **2023**, *8*, 3955−3961.
(37) Chen, B.; Rudd, P. N.; Yang, S.; Yuan, Y.; Huang, J. Imperfections and their passivation in halide perovskite solar cells. *Chem. Soc. Rev.* **2019**, *48*, 3842−3867.
(38) Guo, L.; Liu, X.; Cong, R.; Gao, L.; Zhang, K.; Zhao, L.; Wang, X.; Wang, R. N.; Pan, C.; Yang, Z. Patterned 2D Ferroelectric Perovskite Single-Crystal Arrays for Self-Powered UV Photodetector Boosted by Combining Ferro-Pyro-Phototronic and Piezo-Phototronic Effects. *Nano Lett.* **2022**, *22*, 8241−8249.
(39) Yang, Z.; Lu, J.; ZhuGe, M.; Cheng, Y.; Hu, J.; Li, F.; Qiao, S.; Zhang, Y.; Hu, G.; Yang, Q.; Peng, D.; Liu, K.; Pan, C. Controllable Growth of Aligned Monocrystalline $CsPbBr_3$ Microwire Arrays for Piezoelectric-Induced Dynamic Modulation of Single-Mode Lasing. *Adv. Mater.* **2019**, *31*, 1900647.
(40) Corzo, D.; Wang, T.; Gedda, M.; Yengel, E.; Khan, J. I.; Li, R.; Niazi, M. R.; Huang, Z.; Kim, T.; Baran, D.; Sun, D.; Laquai, F.; Anthopoulos, T. D.; Amassian, A. A Universal Cosolvent Evaporation Strategy Enables Direct Printing of Perovskite Single Crystals for Optoelectronic Device Applications. *Adv. Mater.* **2022**, *34*, 2109862.

https://doi.org/10.1021/acsami.4c00302
ACS Appl. Mater. Interfaces 2024, 16, 16482−16493

(41) Yang, Z.; Wang, H.; Guo, L.; Zhou, Q.; Gu, Y.; Li, F.; Qiao, S.; Pan, C.; Wang, S. A Self-Powered Photodetector Based on $MAPbI_3$ Single-Crystal Film/n-Si Heterojunction with Broadband Response Enhanced by Pyro-Phototronic and Piezo-Phototronic Effects. *Small* **2021**, *17*, 2101572.
(42) Zhang, B.; Yan, J.; Wang, J.; Chen, Y. Effect of the Modulating of Organic Content on Optical Properties of Single-Crystal Perovskite. *Opt. Mater.* **2016**, *62*, 273−278.
(43) Guo, L.; Liu, X.; Gao, L.; Wang, X.; Zhao, L.; Zhang, W.; Wang, S.; Pan, C.; Yang, Z. Ferro-Pyro-Phototronic Effect in Monocrystalline 2D Ferroelectric Perovskite for High-Sensitive, Self-Powered, and Stable Ultraviolet Photodetector. *ACS Nano* **2022**, *16*, 1280−1290.
(44) Liu, Y.; Guo, J.; Zhu, E.; Liao, L.; Lee, S. J.; Ding, M.; Shakir, I.; Gambin, V.; Huang, Y.; Duan, X. Approaching the Schottky-Mott Limit in Van der Waals Metal-Semiconductor Junctions. *Nature* **2018**, *557*, 696−700.
(45) Polat, E. O.; Mercier, G.; Nikitskiy, I.; Puma, E.; Galan, T.; Gupta, S.; Montagut, M.; Piqueras, J. J.; Bouwens, M.; Durduran, T.; Konstantatos, G.; Goossens, S.; Koppens, F. Flexible Graphene Photodetectors for Wearable Fitness Monitoring. *Sci. Adv.* **2019**, *5*, 7846.
(46) You, D.; Xu, C.; Zhang, W.; Zhao, J.; Qin, F.; Shi, Z. Photovoltaic-Pyroelectric Effect Coupled Broadband Photodetector in Self-powered ZnO/ZnTe Core/shell Nanorod Arrays. *Nano Energy* **2019**, *62*, 310−318.
(47) Zhang, Y.; Chen, J.; Zhu, L.; Wang, Z. L. Self-Powered High-Responsivity Photodetectors Enhanced by the Pyro-Phototronic Effect Based on a $BaTiO_3$/GaN Heterojunction. *Nano Lett.* **2021**, *21*, 8808−8816.
(48) Guo, L.; Qi, Y.; Wu, Z.; Yang, X.; Yan, G.; Cong, R.; Zhao, L.; Zhang, W.; Wang, S.; Pan, C.; Yang, Z. A Self-Powered UV Photodetector With Ultrahigh Responsivity Based on 2D Perovskite Ferroelectric Films With Mixed Spacer Cations. *Adv. Mater.* **2023**, *35*, 2301705.
(49) Fu, J.; Ramesh, S.; Melvin Lim, J. W.; Sum, T. C. Carriers, Quasi-Particles, and Collective Excitations in Halide Perovskites. *Chem. Rev.* **2023**, *123*, 8154−8231.
(50) Li, T.; Xu, J.; Lin, R.; Teale, S.; Li, H.; Liu, Z.; Duan, C.; Zhao, Q.; Xiao, K.; Wu, P.; Chen, B.; Jiang, S.; Xiong, S.; Luo, H.; Wan, S.; Li, L.; Bao, Q.; Tian, Y.; Gao, X.; Xie, J.; Sargent, E. H.; Tan, H. Inorganic Wide-Bandgap Perovskite Subcells With Dipole Bridge For All-Perovskite Tandems. *Nat. Energy* **2023**, *8*, 610−620.

https://doi.org/10.1021/acsami.4c00302
ACS Appl. Mater. Interfaces 2024, 16, 16482−16493